Original Article

CAMBRIDGE
UNIVERSITY PRESS

Zircon U–Pb ages, geochemistry and Sr–Nd isotopes of the Golshekanan granitoid, Urumieh–Dokhtar magmatic arc, Iran: evidence for partial melting of juvenile crust

Fatemeh Sarjoughian[1] , Bahareh Zahedi[1], Hossein Azizi[2], Wenli Ling[3], David R. Lentz[4] and Yoshihiro Asahara[5]

[1]Department of Earth Sciences, Faculty of Sciences, University of Kurdistan, Sanandaj, Iran; [2]Department of Mining engineering, Faculty of Engineering, University of Kurdistan, Sanandaj, Iran; [3]Faculty of Earth Sciences, China University of Geosciences, Wuhan 430074, China; [4]Department of Earth Sciences, University of New Brunswick, Fredericton, NB E3B 5A3, Canada and [5]Department of Earth and Environmental Sciences, Graduate School of Environmental Studies, Nagoya University, Nagoya, Japan

Abstract

The Golshekanan granitoid body is situated in the central part of the Urumieh–Dokhtar magmatic arc (UDMA) in central Iran, and includes granite and granodiorite with minor monzonite and diorite. Zircon U–Pb dating yields a late Eocene (Priabonian) crystallization age of 37.6 ± 0.2 Ma. The body is calc-alkaline and metaluminous to weakly peraluminous ($A/CNK \leq 1.10$) with SiO_2 ranging from 61.1 to 71.5 wt% and MgO from 0.8 to 3.3 wt%, with $Na_2O + K_2O$ of 4.0–8.5 wt%. Primitive mantle-normalized trace-element patterns display enrichments in the large-ion lithophile elements (LILE), such as Rb, Cs, Ba and K, and depletion from the high-field-strength elements (HFSEs), such as Nb, Ti, Ta and P. The rocks are enriched in LREEs relative to HREEs (average $(La/Yb)_{CN} = 4.3$) and exhibit weak negative Eu anomalies (average $Eu/Eu^* = 0.75$), revealing typical active continental margin arc affinity. The low initial $^{87}Sr/^{86}Sr$ ratios (0.70440–0.70504) and notable positive $\epsilon_{Nd}(t)$ values (+4.0 to +5.2) indicate an origin by partial melting of juvenile rocks in the lower crust, possibly with some involvement of sub-continental lithospheric mantle beneath Central Iran. These processes probably occurred due to the Neo-Tethys oceanic slab retreat and (or) rollback during late Eocene time.

1. Introduction

The basement of Iran evolved during the late Neoproterozoic – early Cambrian period (610–520 Ma; e.g. Ramezani & Tucker, 2003; Hassanzadeh *et al.* 2008; Rossetti *et al.* 2015; Shabanian *et al.* 2018; Daneshvar *et al.* 2019). This basement resulted from magmatism reflecting subduction of Proto-Tethys oceanic lithosphere beneath northern Gondwana (Ramezani & Tucker, 2003; Hassanzadeh *et al.* 2008). It was also fragmented and drifted from Gondwana as the Palaeo-Tethys and Neo-Tethys oceans opened and later reclosed during the Cambrian–Tertiary period (e.g. Berberian & Berberian, 1981; Şengör, 1987). The closure of the Palaeo-Tethys was completed by the Late Triassic Epoch (e.g. Horton *et al.* 2008), and the opening of the Neo-Tethys was underway by early Permian time (e.g. Alirezaei & Hassanzadeh, 2012).

The Zagros orogen, which resulted from the opening and closure of the Neo-Tethys Ocean, is composed of three NW–SE elongated parallel tectonic zones (Alavi, 1994) that from the Arabian Plate to Central Iran are: (1) the Zagros Simply Folded Belt; (2) the Sanandaj–Sirjan Zone; and (3) the Urumieh–Dokhtar magmatic arc (UDMA) (Fig. 1a). It is attributed to subduction of the western portion of Neo-Tethys oceanic crust and subsequent collision of the Arabian Plate with the eastern Iranian microplate (e.g. Alavi, 1994). The estimates for the time of the Arabia–Eurasia plate collision have been highly controversial, ranging from the Late Cretaceous to the Pliocene epochs. The irregular shape of the Arabian indenter suggests that collision was probably diachronous along the belt (e.g. Agard *et al.* 2005; Ballato *et al.* 2011), which accounts for some of the inconsistency in estimates for collision. Chiu *et al.* (2013) suggested that the oblique collision between Arabia and Eurasia started no later than *c.* 30 Ma (early Oligocene). The collision then propagated SE-wards in the southeastern part by *c.* 10 Ma (late Miocene), when the UDMA magmatism started changing geochemical composition from calc-alkaline to adakitic. Some research (e.g. Ao *et al.* 2016) suggested that final closure of the Neo-Tethys Ocean occurred during the late Miocene Age, whereas others (e.g. Alavi, 1994; Mohajjel *et al.* 2003) suggested that the Urumieh Dokhtar magmatic system is still active and is associated with ongoing subduction of Indian oceanic crust (e.g. Agard *et al.* 2011).
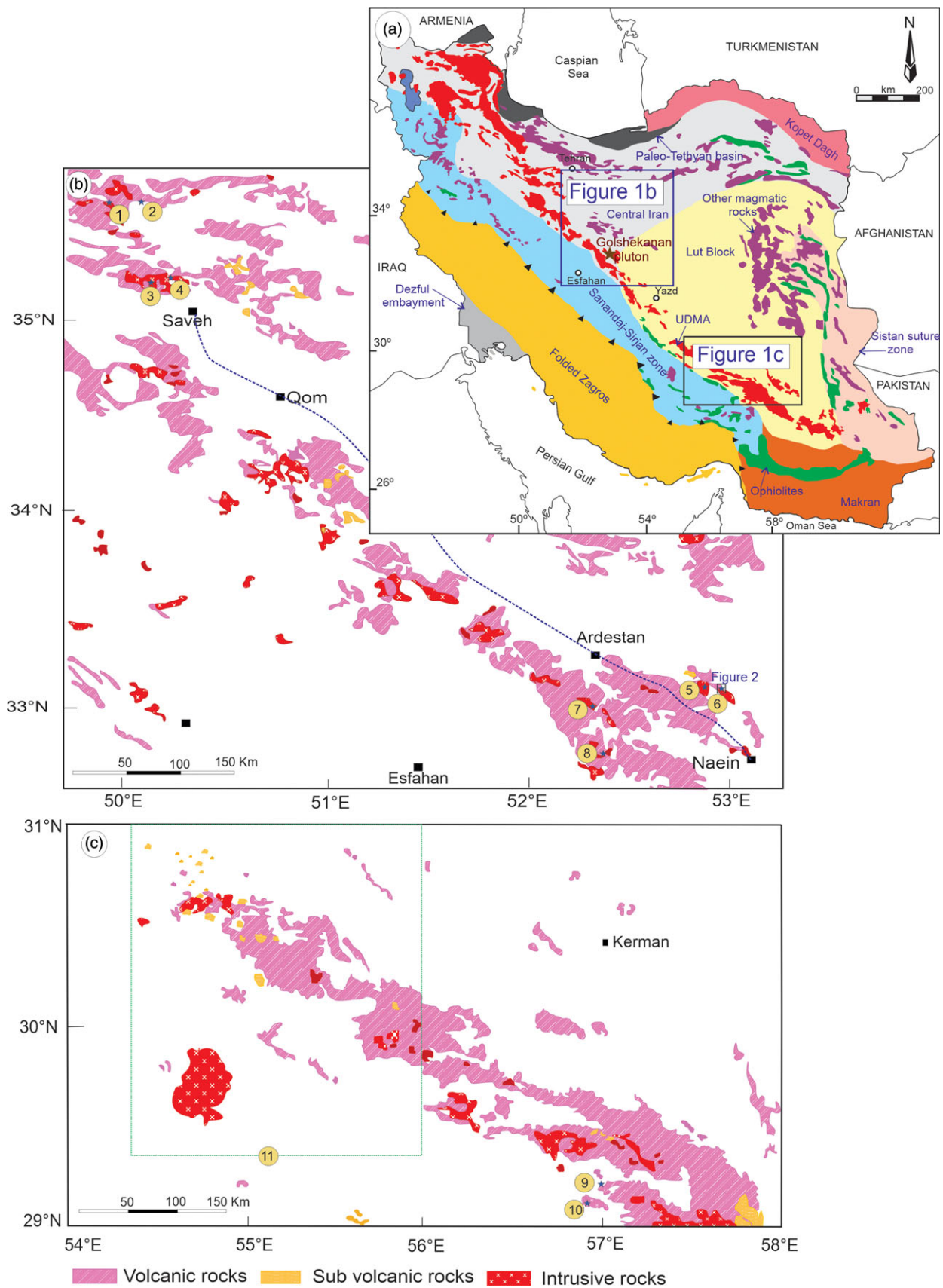
Fig. 1. (Colour online) (a) Simplified geological map of Iran and (b, c) distribution of igneous rocks of Urumieh Dokhtar magmatic belt (UDMA) within it. Location of intrusive rocks and details of age are (1) Haji Abad (40 Ma, Kazemi *et al.* 2019); (2) Gheshlagh–Aftabrow (40 Ma, Kazemi *et al.* 2020), (3) Saveh (40–37 Ma, Nouri *et al.* 2018); (4) Khalkhab–Neshveh (38 Ma, Rezaei-Kahkhaei *et al.* 2011); (5) Soheyle–Pakuh (39.6 Ma, Sarjoughian *et al.* 2020); (6) Golshekanan (37.6 Ma, this study); (7) Zafarghand (24.6 Ma, Sarjoughian & Kananian 2017; Sarjoughian *et al.* 2018); (8) Marshenan (20.5 Ma, Sarjoughian & Kananian 2017; Sarjoughian *et al.* 2019); (9) Sarduiyeh (27.95 Ma, Nazarinia *et al.* 2020); (10) Rabor–Lalehzar (23 Ma, Chekani Moghadam *et al.* 2018); and (11) Kuh–Panj (16.9–12.2 Ma, Asadi, 2018).

The UDMA is located along the northeastern margin of the Zagros orogenic belt, between the Sanandaj–Sirjan zone and Central Iran zone, representing a magmatic belt, which extends along the Sanandaj–Sirjan zone and Central Iranian microcontinent (Alavi, 1994). The UDMA is composed of voluminous mafic to felsic volcanic successions with minor intrusive rocks. The volcanic successions largely comprise calc-alkaline rocks occurring as basaltic and andesitic lava flows, pyroclastic tuffs and ignimbrites (e.g. Stöcklin, 1968; Berberian & Berberian, 1981). The arc volcanism across the UDMA has been argued to be dominated by an Eocene pulse, although Chiu *et al.* (2013, 2017) reported abundant ages that indicate long-lasting magmatic activity, from the Eocene to the Oligocene epochs. The plutonic rocks include gabbroic, dioritic, granodioritic and granitic intrusions of different sizes, ranging in age from Eocene to Miocene (e.g. Chiu *et al.* 2013; Sarjoughian & Kananian, 2017). Geochemical studies indicate that the UDMA is composed of subduction-related calc-alkaline and, to a limited extent, tholeiitic rocks (e.g. Ahmad & Posht Kuhi, 1993), but also with slight alkaline and shoshonitic rocks in the terminal stages (e.g. Ahmadzadeh *et al.* 2010; Sarjoughian *et al.* 2012).

The Golshekanan pluton is located in the central part of the UDMA, and was studied in order to build a better understanding of the magmatic and associated geodynamic evolution of the UDMA. Granitoids provide key clues to understanding Cenozoic magmatism in the UDMA and the growth of continental crust. The UDMA has been the focus of exploration as a result of the high potential of locating porphyry Cu resources. Considering the dual importance of UDMA from geodynamic and metallogenic perspectives, comprehensive petrogenetic studies are fundamental. Although the subduction tectonic context of the UDMA is well constrained, the processes of magma production and source compositions remain controversial. Some researchers (e.g. Asadi, 2018; Deng *et al.* 2018; Wan *et al.* 2018) suggested that the intrusive rocks in the central UDMA were generated from partial melting of juvenile mafic lower crust. However, Honarmand *et al.* (2014), Babazadeh *et al.* (2017, 2019) and Nouri *et al.* (2018) concluded that some magmas were formed from partial melting of asthenospheric mantle and (or) subcontinental lithospheric mantle with or without lower crustal contributions. Detailed studies of individual igneous rocks could therefore be a more appropriate approach to evaluate the origin of the magma.

The Golshekanan pluton belongs to the calc-alkaline series that is similar to an active continental margin setting, and suggests a crustal origin for these rocks (H. Aliashrafzadeh, unpub. MSc thesis, University of Tehran, 2013). Based on the U–Pb method, Sarjoughian & Kananian (2017) show an age of 36.8 ± 0.5 Ma for the Mehrabad intrusion. Although this pluton is not well known, it is studied here in detail for the first time. This research reports new petrographic and geochemical data and U–Pb zircon ages together with Rb–Sr and Sm–Nd data for the Golshekanan granitoid rocks of northern Nain. These data provide insights into: (1) the geochemical characteristics of the source involved in the petrogenesis of UDMA igneous rocks; (2) a petrogenetic model for its generation and emplacement in the framework of the development of the UDMA; and (3) the geodynamic evolution and nature of Cenozoic magmatism across the region.

2. Geological overview

The Golshekanan area is exposed in the central UDMA, in the western part of the Central Iran zone (Fig. 1a) and in the NE of the Esfahan Province, at latitudes 33° 12′–33° 13′ N and longitudes 52° 54′–52° 56′ E (Figs 1b, 2). The basement rocks in this area consist of an ophiolitic mélange complex that is composed of serpentinite, peridotite and minor dunite and pyroxenite, along with radiolarite, limestones and chert. Tertiary magmatic activity can be divided into two main phases: Eocene volcanism with andesite, dacite and rhyolite compositions, including pyroclastic rocks (mainly tuff); followed by emplacement of intermediate to felsic intrusive bodies (Davoudzadeh, 1972; Mansouri Esfahani *et al.* 2017).

The Golshekanan granitoid is exposed as small intrusive bodies in the Mehrabad area, near the western part of the village of Golshekanan. Field observations reveal the studied rocks are mostly medium-grained granite and granodiorite with a minor proportion of monzonite and diorite (Fig. 3a). Porphyritic granodiorite and granite with large feldspar and amphibole phenocrysts also occur. Because of the poor outcrop exposure, the intrusive field relationships cannot be observed. It seems that contacts between granite and granodiorite rocks and porphyritic granodiorite and granite are transitional, and the intrusive bodies may have been rapidly cooled (thermal quenching) at their margin; however, on previous maps a large part of the intrusive rocks was mapped as plutonic rocks (Bahroudi, 1999).

This body is characterized by a smooth rounded morphology and is typically light grey to pink in colour. The pluton hosts a few small xenolith enclaves of the host rocks (Fig. 3b). Additionally, a few mafic doleritic dykes with basalt, andesite and trachyandesite composition cross-cut the Goshekanan granitoid and its peripheral rocks. These dykes are variable in thickness, from a few centimetres to a metre in width.

3. Petrographic features

The studied rocks are mostly granite and granodiorite plus lesser monzonite and diorite varieties. They are composed mainly of quartz, K-feldspar, plagioclase and amphibole, and accessory biotite, zircon, apatite and titanite. The granodioritic rocks contain more plagioclase than the granitic rocks, the monzonite contains more amphibole and less quartz, and diorite has more amphibole and plagioclase, with less quartz and K-feldspar compared with the granites and granodiorites.

These rocks are generally medium-grained and shown granular texture and subordinate granophyre. Plagioclase forms euhedral to subhedral tabular crystals and commonly displays zoning and polysynthetic twinning. Some K-feldspars exhibit Carlsbad twinning and perthitic texture (Fig. 3c). Quartz is anhedral and in part fills interstices between other minerals. Granophyric intergrowths of quartz and alkali feldspar are common, suggesting emplacement at a shallow crustal level. The dominant ferromagnesian phase in these rocks is amphibole and tends to form euhedral to subhedral crystals. Some rocks contain biotite as an accessory phase occurring along the boundaries of K-feldspar and plagioclase, indicating that biotite crystallized later than plagioclase and K-feldspar. Sericite, actinolite, chlorite, calcite, titanite and epidote are also locally present as secondary phases.

In the porphyric granodiorite and granite, K-feldspar, plagioclase, amphibole and quartz are the main constituents and commonly associated with minor biotite, zircon, titanite, apatite and Fe–Ti oxides. They contain abundant amphibole and plagioclase phenocrysts (Fig. 3d). Plagioclase has complex zoning with resorption surfaces and polysynthetic twinning. Quartz and K-feldspar are anhedral and interstitial to the other minerals. Amphiboles occur as euhedral to subhedral tabular-shaped prismatic crystals
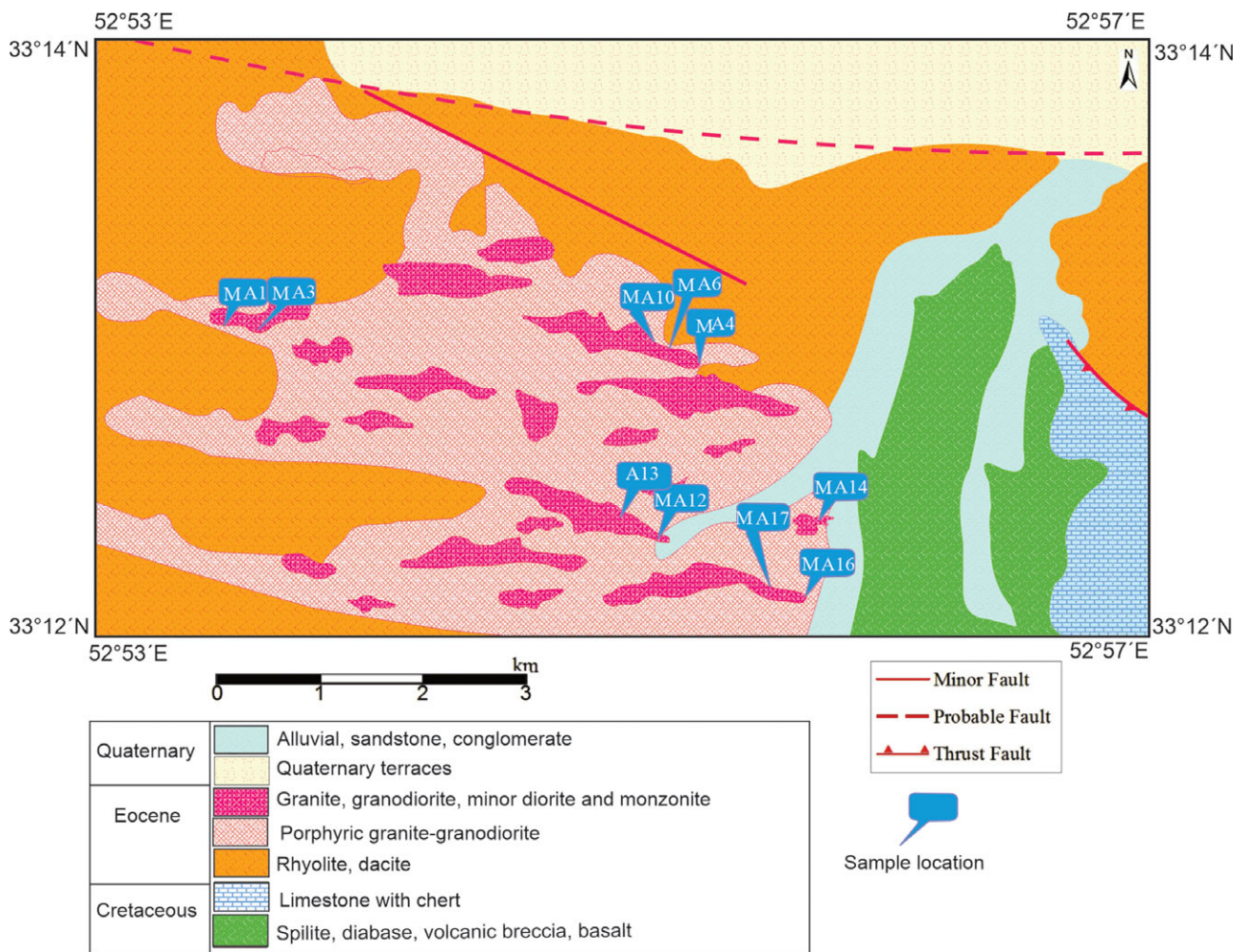
Fig. 2. (Colour online) Regional geological map of the Golshekanan granitoid based on the geological map of Shahrab 1:100 000 (modified after Bahroudi, 1999), with slight modifications.

and show greenish-brown pleochroism. The minor secondary minerals include sericite, chlorite, actinolite, calcite, epidote, titanite and iron oxide.

Dolerite dykes with basalt, andesite and trachyandesite compositions are generally porphyritic and microlitic in texture. Plagioclase and pyroxene are major phenocrysts in these units. Plagioclase, as a phenocryst or a lath-shaped microlite in the groundmass, is ubiquitous. Sieve-textured plagioclase is a common feature. Plagioclase crystals show various amounts of saussuritization. Pyroxene is present as euhedral and subhedral crystals in the basaltic dykes, but is locally altered to epidote, calcite and chlorite. Rarely, anhedral quartz and alkali feldspar occur as aggregates of smaller grains.

4. Analytical methods

A total of 33 samples were collected from representative and least-altered intrusive rocks including dykes. Following petrographic examination, 10 fresh and most representative samples were selected for geochemical analyses.

Granodiorite sample MA1 was selected for zircon dating. The sample (*c.* 3 kg) was crushed and sieved before undergoing magnetic and heavy liquid separation. The analysed zircon grains were hand-picked under a binocular microscope, obtaining highly pure zircon grains (> 99%). About 80 zircon grains were mounted in epoxy together with the standard, and then polished. Zircon grains were studied by cathodoluminescence imaging and analysed for U–Pb isotopes by laser ablation inductively coupled plasma mass spectrometry (LA-ICP-MS) at the State Key Laboratory of Geological Processes and Mineral Resources (GPMR), China University of Geosciences, Wuhan (see Simonetti *et al.* 2006). Detailed operating conditions for the LA system and the ICP-MS instrument and data reduction were described by Liu *et al.* (2008). The weighted mean U–Pb ages were calculated and Concordia plots were constructed using Isoplot 4.1 (Ludwig, 2008).

The samples were analysed for major and trace elements including rare earth elements (REEs) at the ALS Minerals Laboratory in Ireland using fusion ICP-MS and ICP-AES, and also at Nagoya University in Japan using X-ray flourescence (XRF) (Rigaku ZSX PrimusII) and ICP-MS (Agilent 7700×). At ALS Minerals laboratory, samples (0.200 g) for ICP-AES analysis are added to lithium metaborate and/or lithium tetraborate flux (0.90 g), mixed well and fused in a furnace at 1000°C. The resulting melt is then cooled and dissolved in 100 mL of 4% nitric acid and 2% hydrochloric acid. This solution is then analysed by ICP-AES and the results are corrected for spectral inter-element interferences. Oxide concentration is calculated from the determined elemental concentration. In ICP-MS analysis at ALS, samples are added to
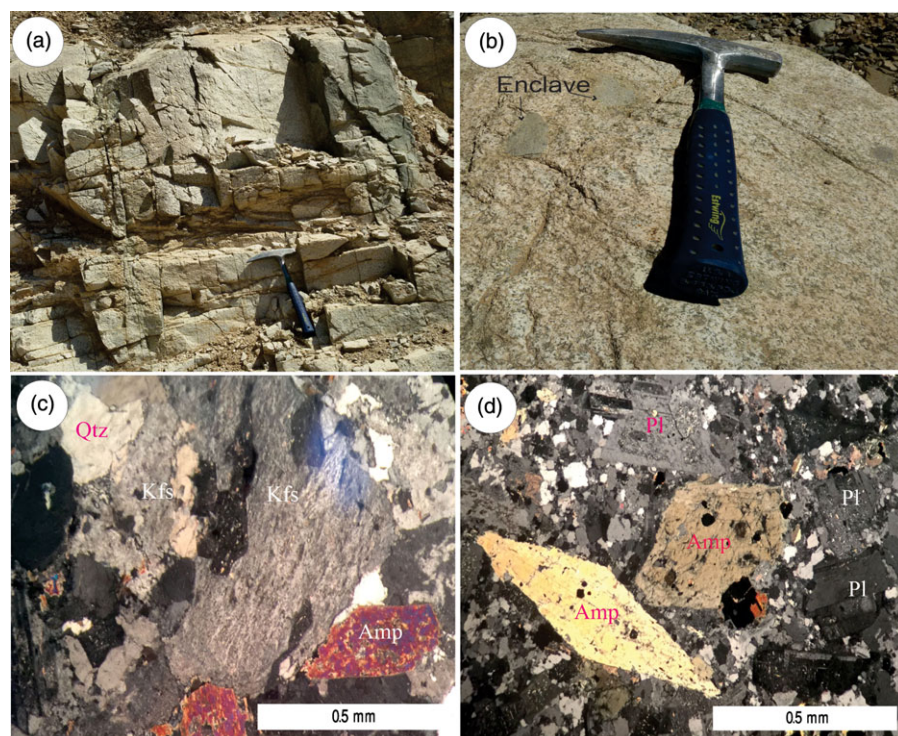
Fig. 3. (Colour online) Field photographs of (a) the Golshekanan granitoid and (b) xenolith enclaves in the host granitoids, and petrographic photographs of (c) porphyritic granodiorite and (d) granite rocks. Mineral abbreviations are from Kretz (1983).

lithium metaborate flux (0.90 g), mixed well and fused in a furnace at 1000°C. The resulting melt is then dissolved in 100 mL of 4% HNO_3 and 2% HCl solution.

At Nagoya University, the major elements were analysed by XRF spectrometry. The glass beads for the XRF analysis were prepared as follows: 0.50 g of sample powder was mixed with 5.0 g of lithium tetraborate, and the mixture was melted at 1200°C for 12–17 min in a high-frequency bead sampler (Rigaku Co. Japan). As for quantitative analysis of trace elements and Sr–Nd isotopic analysis, 50–100 mg of the powder was decomposed in a covered Teflon beaker using 3 mL of HF (38%) and 0.5–1 mL of $HClO_4$ (70%) at 120–140°C on a hot plate in a clean room until the powder was dissolved completely. The dissolved samples were then dried at 140°C on the hot plate using infrared lamps. After drying, the samples were dissolved in 10 mL of 2 M HCl and the residue was completely decomposed in a steel-jacketed bomb at 180°C for 2–5 days.

The Nd and Sr isotopic ratios were analysed using thermal ionization mass spectrometry (TIMS) at GPMR (China) and at Nagoya University (Japan). At GPMR, the sample powders were digested in Teflon bombs using a mixture of double-distilled HNO_3 and HF acids at 190°C for 48 hours. The Sr and Nd elements were separated and purified in a clean laboratory using ion exchange columns of Dowex AG50WX12 cation resin and Eichrom Ln-Spec resin successively. At GPMR the Sr and Nd isotope ratios were measured using a Finnigan Triton TIMS. Isotopic ratios of $^{87}Sr/^{86}Sr$ and $^{143}Nd/^{144}Nd$ were normalized to $^{88}Sr/^{86}Sr = 8.375209$ and $^{146}Nd/^{144}Nd = 0.7219$, respectively. Measurements of standard NIST-SRM987 and La Jolla gave average values of 0.710254 ± 8 ($n = 22$) and 0.511847 ± 3 ($n = 25$) for ratios of $^{87}Sr/^{86}Sr$ and $^{143}Nd/^{144}Nd$, respectively. The initial ratios of $^{87}Rb/^{86}Sr$ and $^{147}Sm/^{144}Nd$ were calculated using Rb, Sr, Nd and Sm concentrations determined by ICP-MS.

At Nagoya University, the isotope ratios of Sr and Nd were measured using a TIMS, VG Sector 54-30 and a GVI IsoProbe-T. The mass fractionations during the Sr and Nd isotope measurements were corrected according to the ratios of $^{86}Sr/^{88}Sr = 0.1194$ and $^{146}Nd/^{144}Nd = 0.7219$, respectively. In this work, NIST-SRM987 and JNdi-1 (Tanaka *et al.* 2000) were adopted as the natural Sr and Nd isotope ratio standards, respectively. During this study, repeated analyses of NIST-SRM987 and JNdi-1 standards gave average values of $^{87}Sr/^{86}Sr = 0.710256 \pm 0.000006$ ($n = 5$) and $^{143}Nd/^{144}Nd = 0.512110 \pm 0.000002$ ($n = 2$), respectively. Detailed descriptions of the quantitative and isotopic analyses in Nagoya University are provided by Azizi & Asahara (2013).

5. Results

5.a. Zircon U–Pb ages

Zircon grains from granodiorite sample (MA1) (Table 1) are mostly pale brown, euhedral to subhedral stubby prisms without any inherited core or new growth rim, and length to width ratios of *c.* 2:1 to 3:1. They have a Th/U ratio > 0.50 (average, 0.66), consistent with a magmatic origin (*cf.* Belousova *et al.* 2002; Kirkland *et al.* 2015).

The results of LA-ICP-MS U–Pb isotopic analyses are presented graphically in Figure 4. Nineteen spots yield constant $^{238}U–^{206}Pb$ ages ranging from 36.1 to 38.9 Ma. The analyses give a weighted mean $^{238}U–^{206}Pb$ age of 37.6 ± 0.2 Ma (mean squared weighted deviation (MSWD), 0.41), which is identical to the concordia age (37.6 ± 0.3 Ma; MSWD, 0.022). The late Eocene (Priabonian) age is consistent with previously published data from other parts of the Mehrabad intrusive rocks (Sarjoughian & Kananian, 2017).

5.b. Whole-rock chemistry

Whole-rock analyses of major and trace elements for all samples are reported in Table 2. The studied samples yielded low loss on ignition (LOI) values (mostly < 3 wt%), indicating low levels of hydrothermal alteration.

Table 1. Zircon U–Pb dating data for the Golshekanan granitoid

| Point	^{232}Th (ppm)	^{238}U (ppm)	Pb (ppm)	^{207}Pb/^{206}Pb	± 1σ	^{207}Pb/^{235}U	± 1σ	^{206}Pb/^{238}U	^{208}Pb/^{232}Th	± 1σ	^{238}U/^{232}Th	^{207}Pb/^{206}Pb age (Ma)	± 1σ	^{207}Pb/^{235}U (age (Ma)	± 1σ	^{206}Pb/^{238}U age (Ma)	± 1σ	^{208}Pb/^{232}Th age (Ma)	± 1σ
Ma1-01	79.5	124	0.88	0.0529	0.0082	0.0379	0.0043	0.0059	0.0018	0.0001	1.700	324	316	37.8	4.2	38.1	1.1	35.5	2.8
Ma1-02	51.3	85.8	0.59	0.0476	0.0076	0.0361	0.0039	0.0056	0.0017	0.0001	1.831	79.7	341	36.0	3.9	36.3	1.1	35.2	2.2
Ma1-03	57.6	93.3	0.65	0.0520	0.0094	0.0372	0.0048	0.0057	0.0020	0.0001	1.776	283	367	37.1	4.7	36.9	1.2	39.6	3.0
Ma1-04	63.1	99.1	0.69	0.0508	0.0106	0.0378	0.0081	0.0059	0.0018	0.0002	1.723	235	422	37.7	7.9	37.7	1.2	36.0	3.2
Ma1-05	56.1	94.6	0.64	0.0517	0.0109	0.0361	0.0064	0.0056	0.0017	0.0002	1.849	333	361	36.0	6.3	36.1	1.4	35.0	3.5
Ma1-06	73.5	116	0.79	0.0491	0.0075	0.0368	0.0040	0.0057	0.0017	0.0001	1.732	150	326	36.7	3.9	36.5	1.3	34.9	2.5
Ma1-09	76.9	128	0.90	0.0493	0.0075	0.0377	0.0040	0.0059	0.0019	0.0001	1.813	161	326	37.6	4.0	37.9	1.4	38.9	2.7
Ma1-10	50.7	81.0	0.57	0.0513	0.0086	0.0379	0.0035	0.0059	0.0018	0.0001	1.745	254	357	37.7	3.5	37.7	1.4	35.8	2.5
Ma1-11	76.9	110	0.76	0.0528	0.0072	0.0373	0.0036	0.0057	0.0019	0.0001	1.553	320	285	37.2	3.5	37.0	1.1	39.0	2.4
Ma1-12	86.5	120	0.86	0.0483	0.0074	0.0385	0.0049	0.0059	0.0016	0.0001	1.536	122	320	38.4	4.8	38.2	1.3	31.8	2.5
Ma1-14	105	177	1.26	0.0494	0.0060	0.0389	0.0033	0.0060	0.0017	0.0001	1.864	169	263	38.7	3.2	38.5	0.9	35.1	1.9
Ma1-16	59.0	110	0.77	0.0491	0.0081	0.0378	0.0058	0.0059	0.0020	0.0002	2.022	150	348	37.7	5.6	37.9	1.5	40.7	3.2
Ma1-17	232	254	1.94	0.0494	0.0065	0.0383	0.0035	0.0060	0.0018	0.0001	1.255	165	291	38.2	3.4	38.4	1.0	35.4	2.1
Ma1-18	108	119	0.87	0.0634	0.0133	0.0380	0.0044	0.0059	0.0018	0.0001	1.247	720	458	37.9	4.3	38.1	1.6	35.9	2.3
Ma1-20	72.0	112	0.82	0.0557	0.0109	0.0381	0.0037	0.0059	0.0021	0.0002	1.697	443	385	38.0	3.6	38.0	1.5	42.4	3.1
Ma1-07	191	248	1.76	0.0495	0.0048	0.0381	0.0031	0.0058	0.0019	0.0001	1.406	172	211	38.0	3.0	37.3	0.9	39.3	1.8
Ma1-08	49.1	85.0	0.60	0.0539	0.0149	0.0398	0.0079	0.0060	0.0017	0.0001	1.898	369	526	39.7	7.7	38.9	1.3	33.9	2.3
Ma1-13	80.9	122	0.85	0.0490	0.0065	0.0369	0.0035	0.0058	0.0019	0.0001	1.697	150	281	36.8	3.5	37.4	1.1	38.6	2.8
Ma1-19	65.6	106	0.78	0.0548	0.0079	0.0394	0.0034	0.0059	0.0022	0.0001	1.769	467	328	39.2	3.3	37.9	1.4	45.0	3.0
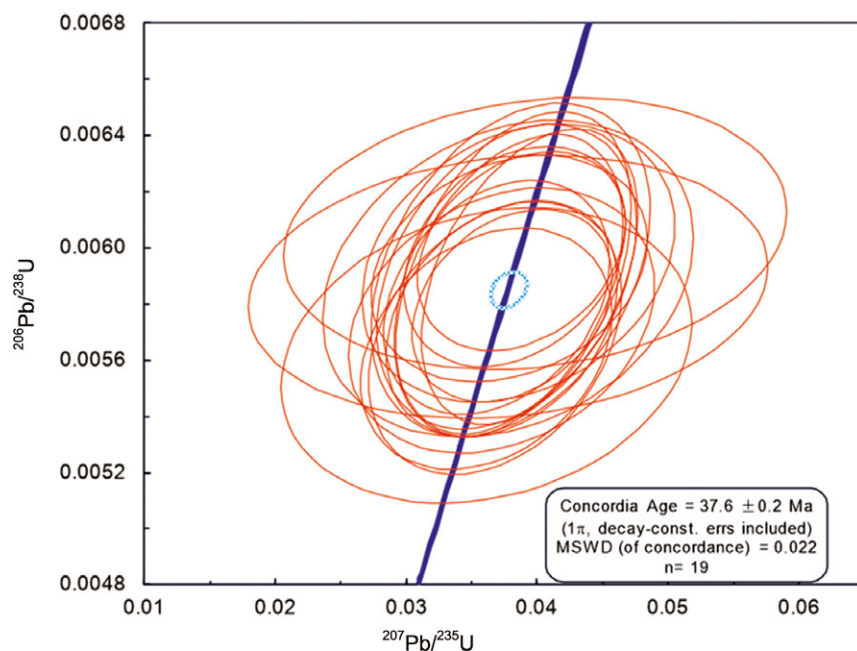
Fig. 4. (Colour online) Concordia diagram for zircon grains (MA1) from the Golshekanan granitoid.

Analyses of this study and the previous data (H Aliashrafzadeh, unpub. MSc thesis, University of Tehran, 2013) indicate that the Golshekanan granitoid can be classified into two groups. In the classification diagram of Middlemost (1994), the intermediate samples plot in the fields of diorite and monzonite, whereas the felsic samples plot in the fields of granodiorite and granite and one dyke plots in the monzogabbro field (Fig. 5).

The Golshekanan granitoid has high contents of SiO_2 (61.1–71.5; average, 66.7 wt%), Al_2O_3 (13.2–16.8; average, 15.4 wt%), and CaO (1.3–7.1; average, 4.5 wt%) and low contents of $Fe_2O_3^T$ (0.3–3.3; average, 1.3 wt%) and MgO (0.8–3.3; average, 1.8 wt%). Most of the samples from the studied granitoid mostly belong to the calc-alkaline series (see Ross & Bedard, 2009; Fig. 6a) and display metaluminous to mildly peraluminous characteristics, with ASI (molar $Al_2O_3/(CaO+K_2O+Na_2O)$) ranging from 0.73 to 1.10, consistent with the lack of typical peraluminous minerals or alkaline mafic minerals. The granitoid samples show I-type affinity according to the classification of Chappell & White (1974) on the A/CNK (molar $Al_2O_3/(CaO+Na_2O+K_2O)$) versus SiO_2 diagram (Fig. 6b).

In the primitive mantle-normalized trace-element spider diagram (Sun & McDonough, 1989) (Fig. 7a), most of the samples display trace-element patterns, marked by enrichment by large-ion lithophile elements (LILE), such as Cs, Ba and K, and the depletion of high-field-strength elements (HFSE), such as Nb, Ta, Ti and P. These features are recognized as a fingerprint of subduction-related magmas (e.g. Wilson, 1989; Pearce, 1996). In chondrite-normalized rare earth element (REE) plot (Sun & McDonough, 1989; Fig. 7b) the samples have a relatively homogeneous pattern, with an enrichment of light REEs (LREE) and heavy REEs (HREE) by a factor of approximately 20–100 and 10–20, respectively. They also show LREE enrichment relative to HREE (La_N/Yb_N = 1.66–8.14) and flat HREE (Gd_N/Yb_N = 0.90–1.31) with negative Eu anomalies (average Eu/Eu* = 0.75), except one sample with Eu/Eu* = 1.02.

5.c. Whole-rock Sr–Nd isotope ratios

Eight whole-rock samples were analysed for Rb–Sr and Sm–Nd isotopic compositions (Table 3). As illustrated in Figure 8, the samples mostly plot along the bulk earth vertical line and in the right quadrants of a conventional Sr–Nd isotope diagram. Initial $^{87}Sr/^{86}Sr$ ratios and $\epsilon_{Nd}(t)$ values were calculated using the age of 37.6 Ma. The initial $^{87}Sr/^{86}Sr$ ratios range from 0.70440 to 0.70504, $^{143}Nd/^{144}Nd_{(t)}$ ratios range from 0.51279 to 0.51286, and the $\epsilon_{Nd}(t)$ values are positive in all cases, ranging from +4.0 to +5.2.

6. Discussion

6.a. Petrogenesis

The Golshekanan granitoid body has I-type calc-alkaline arc signatures. The following three models, or some combination of them, could account for the formation of these rocks: (1) fractional crystallization of peridotite mantle-derived melts with and (or) without contamination (e.g. Soesoo, 2000); (2) partial melting of old mafic to intermediate meta-igneous crust (e.g. Roberts & Clemens, 1993); and/or (3) partial melting of juvenile crust (e.g. Xiao *et al.* 2007; Peng *et al.* 2014; Zhao *et al.* 2015).

The first model is not favoured for the Golshekanan granitoid, because felsic magmas are voluminous (> 95%) relative to intermediate magma. It has high SiO_2 contents, with low MgO, Cr and V contents compared with magmaic rocks that would be derived by partial melting of the mantle (e.g. van Middelaar & Keith, 1990).

A very low-degree hydrous partial melting of mantle could produce andesitic melts, but to produce high volumes of felsic magma is physically difficult and practically unlikely (e.g. Mo *et al.* 2007). Moreover, there are no contemporary mafic volcano-plutonic complexes in the studied area. The variations in incompatible element ratios potentially indicate that they can be generated by

Table 2. Data for major (wt%) and trace elements (ppm) of Golshekanan granitoids. gr – granite; gd – granodiorite; di –diorite; dk – dolerite dyke

Sample	MA3[a]	MA4[a]	MA6[a]	MA10[a]	MA12[a]	MA14[a]	MA16[a]	MA17[a]	MA1[b]	MA13[b]
Type	gd	di	gd	gd	gr	dk	gr	gd	gd	gd
SiO_2	69.90	61.10	67.90	66.20	68.50	48.70	66.80	68.90	66.03	65.51
TiO_2	0.40	0.46	0.38	0.38	0.32	1.01	0.43	0.64	0.43	0.46
Al_2O_3	15.55	15.90	15.35	15.30	14.75	16.45	16.05	13.20	16.75	15.14
Fe_2O_3	0.36	1.91	0.63	0.87	1.26	3.73	0.34	0.59	0.62	1.38
FeO	0.60	2.62	1.04	1.58	1.43	6.58	0.40	0.76	1.02	2.28
MnO	0.03	0.12	0.06	0.07	0.07	0.74	0.05	0.07	0.04	0.11
MgO	1.52	3.04	1.26	1.40	1.27	6.91	1.70	1.00	1.77	1.85
CaO	7.12	3.08	5.69	6.95	1.29	5.70	5.05	3.88	5.96	5.62
Na_2O	4.28	5.44	4.51	3.79	4.34	3.45	7.13	6.76	4.61	4.39
K_2O	0.20	1.24	0.19	0.24	3.65	1.82	0.54	0.01	0.26	0.43
P_2O_5	0.14	0.14	0.11	0.11	0.11	0.29	0.15	0.16	0.14	0.14
LOI	0.43	3.01	0.84	0.88	1.33	4.90	1.69	3.80	1.10	0.99
Total	100.68	98.46	98.16	98.04	98.63	101.22	100.45	99.87	98.84	98.56
V	72	114	80	86	53	311	78	45	89.7	108
Cr	50	20	10	7	10	50	20	20	31	39
Ga	15.2	13.2	14.4	15.3	11.9	18.1	14.6	8.2	15.4	15.3
Rb	3.30	28.00	3.60	3.80	72.70	31.10	12.60	1.40	4.23[b]	7.36[b]
Sr	631	320	677	630	382	398	544	105	675	636
Zr	157	71	140	124	101	56	123	203	106	92
Hf	4.30	2.20	4.00	3.60	2.90	1.80	3.40	5.40	3.46	3.04
Nb	4.70	2.70	4.90	4.10	4.10	3.00	3.70	6.50	4.35	4.22
Cs	0.20	0.43	0.14	0.10	0.76	0.36	0.26	0.11	0.17	0.20
Ba	95.1	321	83.9	94.8	849	820	63.7	14.9	127	137
Th	8.55	5.66	10.05	8.81	8.64	1.96	5.15	6.34	7.40	7.35
U	1.55	1.56	2.65	2.34	2.43	0.55	0.80	1.70	1.79	1.99
Ta	0.60	0.40	0.60	0.50	0.50	0.30	0.50	0.60	0.52	0.41
Y	16.6	13.3	18.6	13.8	10.8	18.1	16.3	23.3	14.7	16.5
La	8.6	12.8	16.1	11.4	7.5	11.7	4.7	9.7	21.0[b]	17.6[b]
Ce	23.5	23.2	31.7	21.9	14.5	24.3	13.4	21.5	39.2	33.8
Pr	3.22	2.69	3.84	2.55	1.85	3.19	2.17	2.97	4.13	3.91
Nd	12.8	10.7	14.5	10.3	6.8	14.6	10.1	12.2	15.5	15.2
Sm	2.94	2.54	3.32	2.17	1.85	3.95	2.78	3.30	2.86	3.21
Eu	0.82	0.82	0.96	0.76	0.57	1.27	0.68	0.43	0.83	0.79
Gd	2.95	2.39	3.03	2.34	1.66	4.04	3.08	3.43	2.74	3.10
Tb	0.46	0.41	0.47	0.37	0.27	0.56	0.50	0.61	0.42	0.45
Dy	2.63	2.20	2.89	2.26	1.72	3.43	3.00	3.94	2.57	2.84
Ho	0.57	0.48	0.63	0.47	0.36	0.67	0.57	0.77	0.54	0.62
Er	1.67	1.43	1.83	1.53	1.06	2.05	1.79	2.68	1.62	1.77
Tm	0.27	0.23	0.29	0.25	0.18	0.27	0.28	0.43	0.27	0.27
Yb	2.06	1.66	2.12	1.60	1.28	1.57	1.92	3.07	1.75	1.91
Lu	0.31	0.25	0.34	0.27	0.22	0.25	0.29	0.45	0.27	0.30

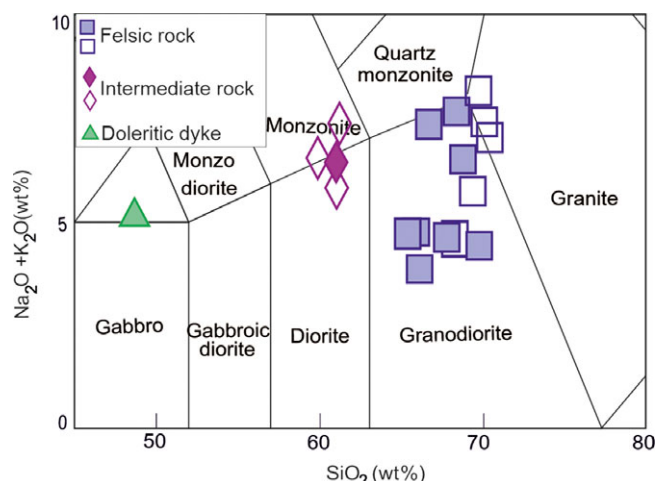[a]ALS Minerals Laboratory (Ireland); [b]Nagoya University (Japan).

Fig. 5. (Colour online) Chemical classification diagram of Middlemost (1994). The studied samples plot in the granite, granodiorite, diorite and monzonite fields. Square – felsic rocks; diamond – mafic-intermediate. Open symbols are from H. Aliashrafzadeh (unpub. MSc thesis, University of Tehran, 2013).
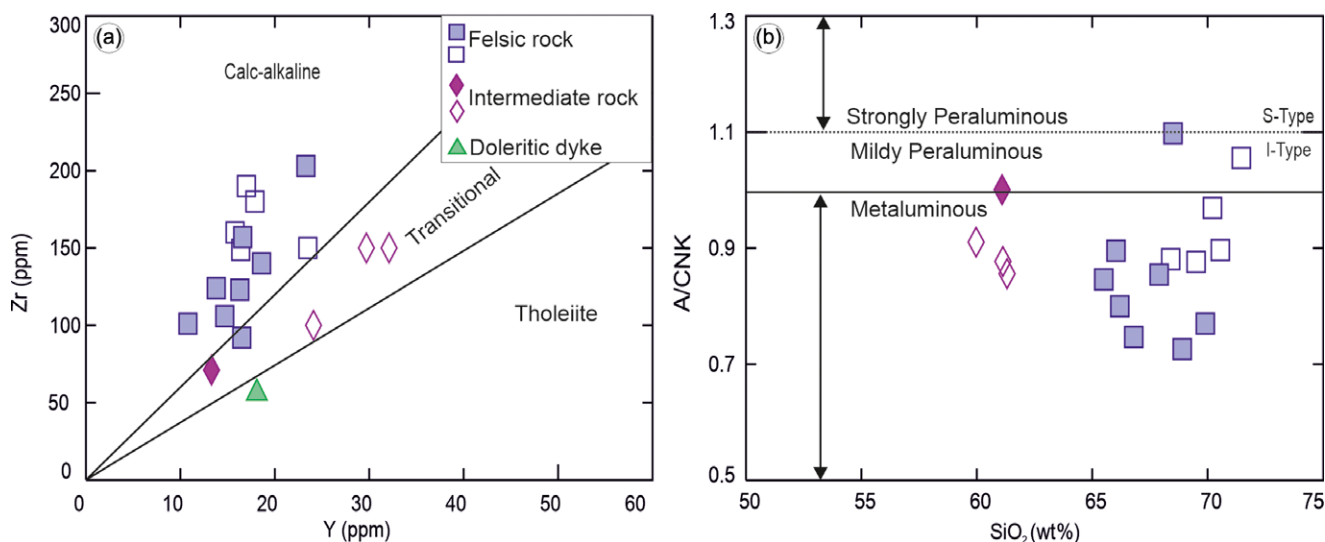

Fig. 6. (Colour online) (a) Zr versus Y (Ross & Bédard, 2009) and (b) A/CNK versus SiO_2 (Chappell & White, 1974) diagrams, indicating that most of the samples are calc-alkaline and metaluminous.
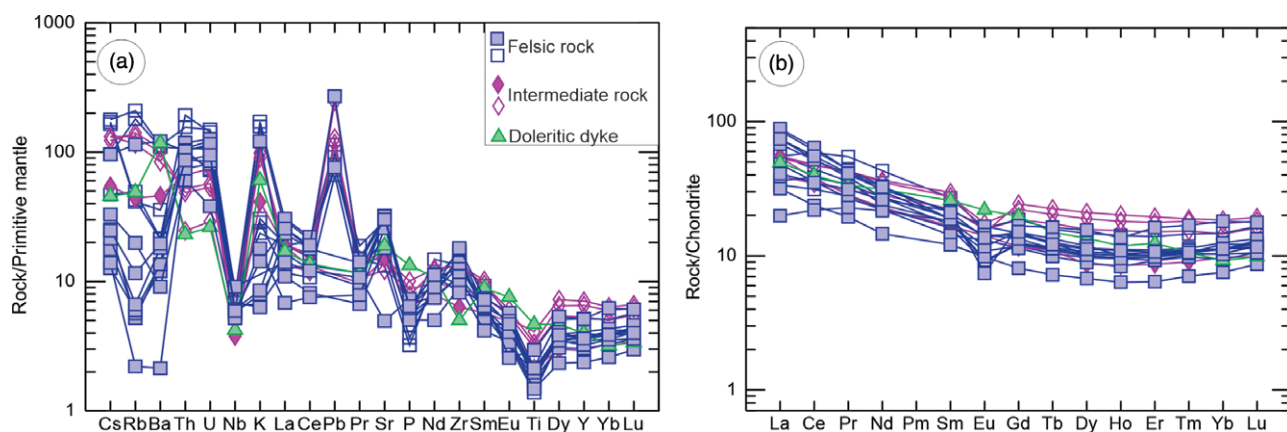

Fig. 7. (Colour online) (a) Primitive mantle-normalized spider diagrams and (b) chondrite-normalized REE patterns for representative samples of the Golshekanan granitoid. Normalization values from Sun & McDonough (1989).

Table 3. Sr and Nd isotopic ratios from the Golshekanan granitoids

Sample	$^{87}Rb/^{86}Sr$	$^{87}Sr/^{86}Sr$	$\pm 1\sigma$	$^{147}Sm/^{144}Nd$	$^{143}Nd/^{144}Nd$	$\pm 1\sigma$	$^{87}Sr/^{86}Sr(i)$	$^{143}Nd/^{144}Nd(t)$	$\epsilon_{Nd}(t)$	T_{DM1} (Ma)	$f_{Sm/Nd}$
G25[a]	0.766	0.704805	0.000007	0.161	0.512876	0.000005	0.70440	0.51284	4.8	795	−0.18
G27[a]	0.611	0.704891	0.000004	0.155	0.512895	0.000003	0.70456	0.51286	5.2	659	−0.21
G39[a]	0.980	0.704974	0.000007	0.123	0.512822	0.000008	0.70445	0.51279	3.9	554	−0.37
G40[a]	0.112	0.705044	0.000007	0.142	0.512828	0.000006	0.70498	0.51279	4.0	687	−0.28
G42[a]	0.163	0.705122	0.000006	0.148	0.512836	0.000005	0.70504	0.51280	4.1	728	−0.25
G36[a]	0.147	0.704884	0.000006	0.124	0.512833	0.000006	0.70481	0.51280	4.2	541	−0.37
MA1[b]	0.018	0.704907	0.000006	0.112	0.512844	0.000004	0.70490	0.51282	4.4	458	−0.43
MA13[b]	0.033	0.704985	0.000007	0.128	0.512845	0.000004	0.70497	0.51281	4.4	543	−0.35

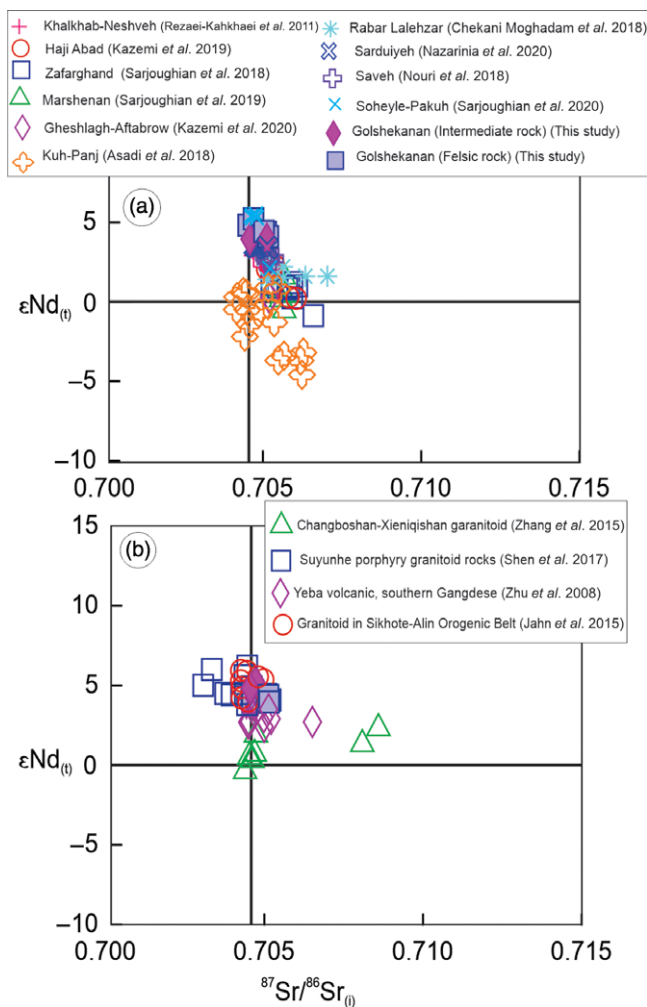[a]GPMR (China); [b]Nagoya University (Japan).

Fig. 8. (Colour online) $^{87}Sr/^{86}Sr_{(i)}$ versus $\epsilon_{Nd}(t)$ diagram indicates the source of the magma from the Golshekanan granitoid and is compared with (a) other igneous provinces in the UDMA and (b) other cogenetic suites over the world.

The uniform zircon and lack of inherited zircons in the studied samples probably indicate that crustal contamination is relatively insignificant during ascent and emplacement of the Golshekanan granitoid (Li et al. 2012).

Most of the Golshekanan granitoid rocks have MgO < 2 wt%, CaO > 2 wt%, FeO$_T$ > 2 wt% and TiO$_2$ < 1.0 wt%. These features are emulated in high temperature melting experiments (1000°C) using amphibolite as the starting material (e.g. Beard & Lofgren, 1991; Rapp & Watson, 1995). It is postulated that entrainment of peritectic phases may produce magmas more mafic than granite (Clemens et al. 2011; Clemens & Stevens, 2012), similar to some of the studied samples. The low K$_2$O/Na$_2$O value rules out an affinity to meta-pelitic, meta-greywacke and meta-andesitic sources (Fig. 10a; Patiño Douce, 1999). These features are analogous to those of the Cordilleran calc-alkaline granites resulting from partial melting of a meta-basaltic source (Patiño Douce, 1999). Variation in SiO$_2$ and Al$_2$O$_3$ also point to magma generated from H$_2$O undersaturated basaltic amphibolite at low pressures (Fig. 10b; Gürsu, 2016). Large proportions of meta-basaltic continental lower crust have a composition similar to that of amphibolite facies metamorphic terrains (Hacker et al. 2015).

Wyllie & Wolf (1993) and López & Castro (2001) have experimentally shown that amphibolites start to melt at relatively high temperatures (800–900°C) at pressures < 1 GPa, while dehydration melting commences at temperatures as low as 750°C at < 1 GPa. The experimental data recommend that the partial melting of the mafic lower crust could produce melts of metaluminous composition irrespective of the degree of the partial melting, and less silicic melts were derived from high degrees of partial melting in the lower crust (e.g. Rushmer, 1991; Rapp & Watson, 1995). It is concluded that the Golshekanan granitoid magma was initially generated from low-pressure partial melting in the plagioclase stability field, which is also confirmed by Al$_2$O$_3$/(FeO$_T$+MgO+TiO$_2$) versus Al$_2$O$_3$+MgO+TiO$_2$+FeO$_T$ discrimination diagram (Fig. 10c; Douce, 1999).

The (La/Yb)$_N$ values in the Golshekanan samples are lower than those in magma derived from a source with garnet as the major phase ((La/Yb)$_N$ < 20), although low Yb (average, 2.1 ppm) and Y (average, 18.9 ppm) of the studied rocks could show the presence of residual hornblende in the source (e.g. Martin, 1987; Tang et al. 2017). In conclusion, the weak HREE fractionation and also negative Eu anomalies suggest a residual plagioclase + hornblende + pyroxene assemblage without garnet in the melting region (e.g. Guo et al. 2009).

variable degrees of partial melting or by fractional crystallization. In the diagrams of La versus La/Sm (e.g. Zhao et al. 2015) and versus La/Yb (e.g. Jiang et al. 2014) (Fig. 9), the data display a clear ascending trend, indicating that the magma was dominantly controlled by partial melting and not by fractional crystallization.
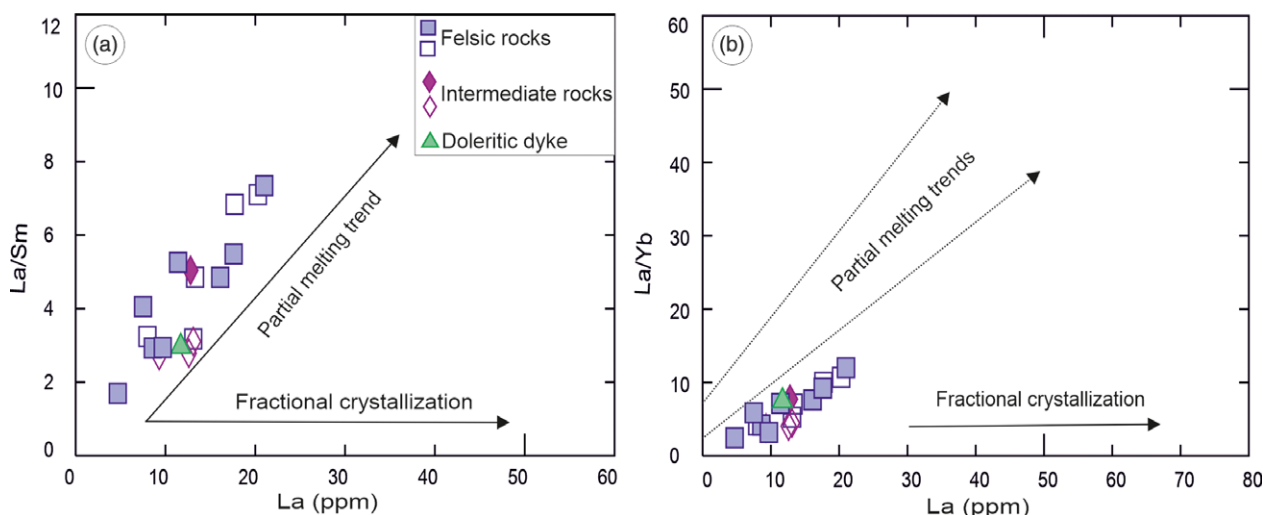
Fig. 9. (Colour online) La against (a) La/Sm and (b) La/Yb diagrams, illustrating trends of partial melting against fractional crystallization processes.
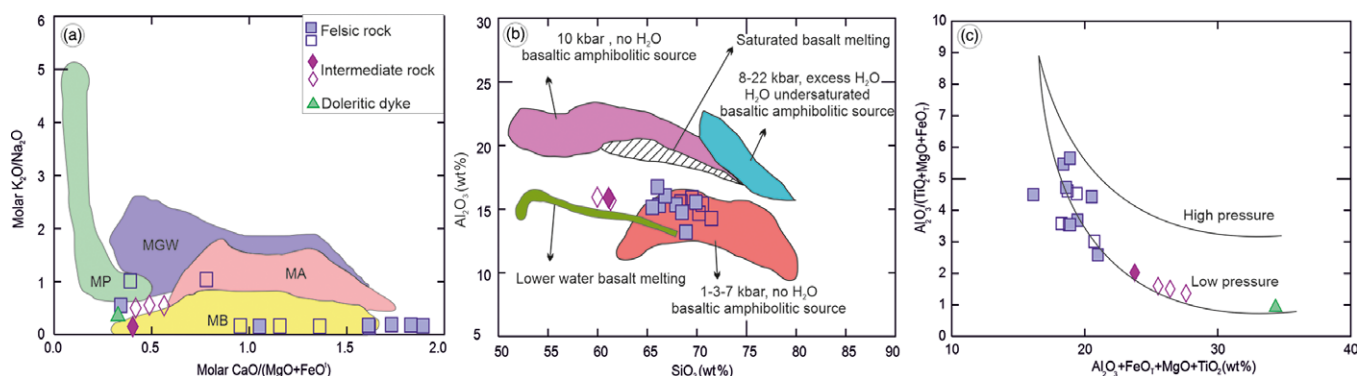

Fig. 10. (Colour online) Molar (a) K_2O/Na_2O versus $CaO/(MgO+FeO_T)$ (Patiño Douce, 1999); (b) Al_2O_3 versus SiO_2 (Gürsu, 2016); and (c) $Al_2O_3/(FeO_T+MgO+TiO_2)$ versus $Al_2O_3+MgO+TiO_2+FeO_T$ (Douce, 1999) diagrams for samples from the Golshekanan granitoid. MB – metabasalt; MA – meta-andesite; MGW – metagreywacke; MP – metapelite. Data from Patiño Douce (1999).

The above discussion proposes that the Golshekanan granitoid magma was generated in lower crust, but there are two different types of lower crust in orogenic belts, that is, ancient basement and more juvenile crusts. According to the tracer isotopic results, these granitoid melts are partial melts of juvenile crust; perhaps this juvenile source is the mixing product between juvenile and ancient basement crust during the Neo-Tethyan subduction.

In comparison with the igneous rocks equivalents from the UDMA, the Sr–Nd isotopic composition of the studied rocks is relatively similar to those from Khalkhab–Neshveh (Rezaei-Kahkhaei *et al.* 2011), Haji Abad (Kazemi *et al.* 2019), Gheshlagh–Aftabrow (Kazemi *et al.* 2020), Saveh (Nouri *et al.* 2018), Zafarghand (Sarjoughian *et al.* 2018), Marshenan (Sarjoughian *et al.* 2019), Soheyle–Pakuh (Sarjoughian *et al.* 2020), Rabor–Lalehzar adakitic (Chekani Moghadama *et al.* 2018), Sarduiyeh (Nazarinia *et al.* 2020) and Kuh–Panj (Asadi, 2018). Most of the data lie well above the right quadrant of the Sr–Nd diagram (Fig. 8a). Geological characteristics of intrusive rocks elsewhere in the UDMA are noteworthy (see Table 4).

Data for some subduction-related, cogenetic rocks from around the world also compare to the two Golshekanan granitoid phases (Fig. 8b). The Golshekanan isotopic signatures are similar to

juvenile crust-derived granitoids rocks, as found in some parts of China and Russia (e.g. Jahn *et al.* 2000a, b; Kröner *et al.* 2014).

The positive $\epsilon_{Nd}(t)$ can be produced by partial melting of juvenile lower crust, such as arcs, ophiolites and accretionary complexes (e.g. Gromet & Silver, 1987; Wu *et al.* 2000). The juvenile crustal components in arc systems can be sourced either from crustal underplating during extension or from partial melting of a subducted oceanic crust (Zhang *et al.* 2016). However, significant oceanic slab partial melting is precluded by the low Sr/Y (average, 27.3) and La/Yb (average, 6.4) values.

To evaluate, a simple mixing model was applied (Fig. 11). We assume that the Golshekanan granitoid formed through magma mixing processes involving the juvenile magmas incorporating either old lower continental crustal (LCC) or upper continental crustal (UCC) material. We are use typical LCC compositions from Taylor & McLennan (1985) and UCC compositions from Rudnick & Fountain (1995). It would be better to use the juvenile end-members that have been reported for Cadomian rocks from Iran, with an end-member from Sabzevar ophiolite (Shafaii Moghadam *et al.* 2014).

The modelling calculation results suggest that a considerable proportion of juvenile crust (c. 90–95%) and slight ancient lower

Table 4. Geological characteristics and ages of intrusions elsewhere in the UDMA

| Name	Latitude (N)	Longitude (E)	Type rocks and field observation	Age (Ma)	Reference
Khalkhab–Neshveh	35° 06′–35° 12′	50° 04′–50° 18′	Quartz monzogabbro, quartz monzodiorite, tonalite, granodiorite and granite	38	Rezaei-Kahkhaei *et al.* (2011)
Haji Abad	35° 32′–35° 37′	49° 50′–50° 05′	Granodiorite and diorite with mafic microgranular enclaves	40	Kazemi *et al.* (2019)
Zafarghand	33° 00′–33° 12	52° 18′–52° 30′	Diorite, granodiorite, granite and rare gabbro with mafic microgranular enclaves	24.6	Sarjoughian *et al.* (2018)
Marshenan	32° 50′–32° 53′	52° 21′–52° 26′	Granodiorite and diorite and rare granite and gabbro with mafic microgranular enclaves	20.5	Sarjoughian *et al.* (2019)
Geshlagh–Aftabrow	35° 27′–35° 30′	50° 02′–50° 05′	Granodiorite with mafic microgranular enclaves	40	Kazemi *et al.* (2020)
Kuh–Panj	28° 00′–31° 00′	54° 15′–58° 30′	Quartz monzonite, tonalite, granodiorite and diorite	16.9–12.2	Asadi (2018)
Rabar–Lalehzar	29° 15′–29° 30′	56° 45′–57° 00′	Granites, granodiorites and diorites	23.2	Chekani Moghadam *et al.* (2018)
Sarduiyeh	29° 15′–29° 30′	57° 10′–57° 25′	Diorite, tonalite, granodiorite and monzogranite	27.95	Nazarinia *et al.* (2020)
Saveh	35° 06′–35° 12′	50° 00′–50° 16′	Granodiorite, tonalite, diorite and minzodiorite	40–37	Nouri *et al.* (2018)
Soheye–Pakuh	33° 09′–33° 12′	52° 09′–53° 03′	Quartz diorite, quartz monzodiorite, tonalite, granodiorite and granite	39.6	Sarjoughian *et al.* (2020)
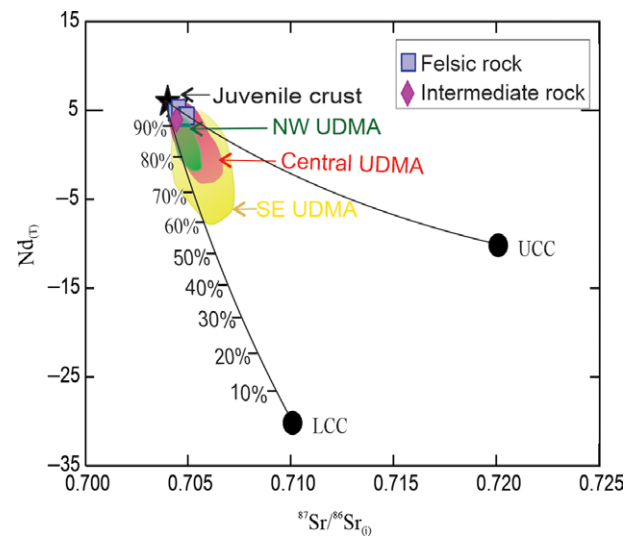
Fig. 11. (Colour online) $\epsilon_{Nd}(t)$ versus $^{87}Sr/^{86}Sr_{(i)}$ isotopic modelling results for the Golshekanan granitoid and adjacent fields in the UDMA. Parameters for Sr–Nd isotopic modelling are from Sabzevar ophiolite (Shafaii Moghadam *et al.* 2014), lower crust (Taylor & McLennan, 1985) and upper crust (Rudnick & Fountain, 1995). NW UDMA including: Haji Abad (Kazemi *et al.* 2019), Khalkhab–Neshveh (Rezaei-Kahkhaei *et al.* 2011), Saveh (Nouri *et al.* 2018) and Gheshlagh–Aftabrow (Kazemi *et al.* 2020). Central UDMA including: Marshenan (Sarjoughian *et al.* 2019), Zafarghand (Sarjoughian *et al.* 2018) and Soheyle–Pakuh (Sarjoughian *et al.* 2020). SE UDMA including: Rabor–Lalehzar (Chekani Moghadam *et al.* 2018), Sarduiyeh (Nazarinia *et al.* 2020) and Kuh-Panj (Asadi, 2018).

crustal components (*c.* 5–10%) were involved in the magma formation. We also used Sr–Nd isotope data on other intrusive rocks in the UDMA. As shown in Figure 11, the isotope modelling results are similar to Golshekanan granitoid with 60–95% mantle-derived juvenile crustal composition with crustal contamination. It is of course highly possible that other parameters, such as the mantle source (asthenospheric versus lithospheric, mantle wedge, etc.) could have affected our results.

6.b. Paleocene magmatism in the UDMA

The Palaeogene–Neogene magmatic flare-up was one of the most significant magmatic events in the UDMA, which occurred during 53.9–5.3 Ma (e.g. Chiu *et al.* 2017; Sarjoughian & Kananian, 2017; Babazadeh *et al.* 2019) within an Andean-type belt. The isotopic signature of the Golshekanan granitoid rocks is compared with that of well-known igneous rocks from UDMA (Fig. 1b, c). The Golshekanan granitoid and adjacent igneous rocks in the UDMA have almost similar major- and trace-element contents. Isotopically, almost all data lie well above quadrants near and along the bulk earth vertical line of a conventional Sr–Nd isotope diagram (Fig. 8a). The Golshekanan granitoid has significantly higher $\epsilon_{Nd}(t)$ values and lower $^{87}Sr/^{86}Sr_{(i)}$ ratios than the Kuh–Panj (Asadi, 2018), Zafarghand (Sarjoughian *et al.* 2018) and Marshenan (Sarjoughian *et al.* 2019) intrusions. It also has slightly higher $\epsilon_{Nd}(t)$ values and lower $^{87}Sr/^{86}Sr_{(i)}$ ratios than the Khalkhab–Neshveh (Rezaei-Kahkhaei *et al.* 2011), Haji Abad (Kazemi *et al.* 2019), Gheshlagh–Aftabrow (Kazemi *et al.* 2020), Saveh (Nouri *et al.* 2018), Sarduiyeh (Nazarinia *et al.* 2020) and Rabar–Lalehzar (Chekani Moghadam *et al.* 2018), and is similar to Soheyle–Pakuh (Sarjoughian *et al.* 2020) (Fig. 8a). The similar isotopic signatures reveal the interaction of mantle-dominant juvenile melts with a greater contribution of old lower continental
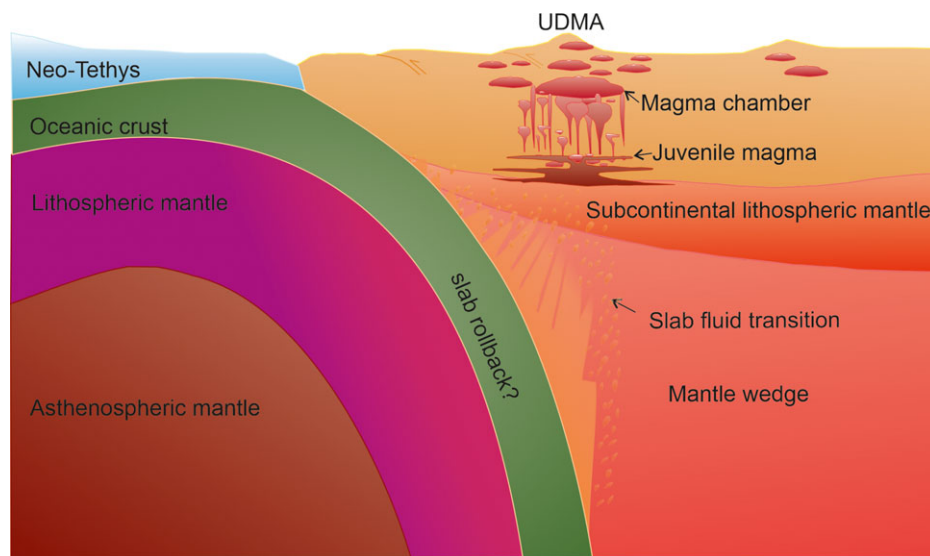
Fig. 12. (Colour online) Schematic geodynamic model for the tectonic evolution of subduction of Neo-Tethys oceanic lithosphere under the Iranian continental plate and development of igneous rocks in the UDMA. The metasomatized mantle upwelling and lithospheric extension activities caused partial melting of mantle-derived juvenile lower crust rocks to generate the late Eocene Golshekanan in the UDMA (see text for the details).

crust, where undoubtedly mantle material was injected into the magma. Deng *et al.* (2018) postulated that most of the reported igneous rocks from the UDMA have intermediate to felsic compositions and only small volumes of mafic rocks, with low MgO, Cr and Ni values, inconsistent with the compositional characteristics of mantle source rocks. The partial melting of a mafic lower crust is therefore a more plausible mechanism for the generation of the UDMA. The Sr–Nd isotope compositions of samples from the UDMA are close to the CHUR (chondritic uniform reservoir) composition, which can also be regarded as the isotopic characteristics of the juvenile source, which could record Cambrian–Neoproterozoic crustal growth in the area.

The thermal anomaly associated with widespread upwelling of mantle caused selective and localized partial melting of juvenile crust to produce the melts in the UDMA during the Eocene–Miocene epochs.

6.c. Geodynamic implications and tectonic setting

Subduction of the Proto-Tethys underneath the Gondwana margin caused mantle-derived basaltic magmas to intrude the lower crust during Ediacaran–early Cambrian time, making the mafic juvenile lower crust of the UDMA.

During the late Eocene – Miocene period, the mantle upwelling in the UDMA responsible for partial melting of the juvenile lower crust in the extensional environment, as a result of oblique subduction (local transpression), might be a valid mechanism to produce the Golshekanan granitoid and nearby intrusive rocks under locally extensional tectonics. The Cenozoic extension was related to the steepening dip of the Neotethyan slab and trench rollback (e.g. Sepidbar *et al.* 2019). Slab rollback is a mechanism suggested to have caused Palaeogene magmatism throughout the UDMA during the transition from a compressional to an extensional convergent plate margin. The rollback followed a period of subduction, analogous to the Laramide and post-Laramide evolution of the western USA.

In Iran, during the closure of the Neo-Tethys basin, middle Eocene – early Oligocene extension and lithospheric thinning might have been accompanied by decompression melting of upwelling hydrous mantle (Verdel *et al.* 2011). The extension may also have been accompanied by lithospheric delamination

(e.g. Haschke *et al.* 2010; Shomali *et al.* 2011; Ahmadian *et al.* 2016), further initiating extension and rapid exhumation of the central Iranian core complexes (e.g. Sepidbar *et al.* 2018).

Consequently, we postulate that the subduction of the Neo-Tethys in the UDMA may have been initiated during early Cenozoic time and the shallow dip of the slab penetrated the mantle beneath the central Iran microcontinent. With significantly enhanced convergence rates during Cenozoic time, the subducted slab descended more rapidly with a steeper dip, resulting in decompression melting and an influx of mantle magma with slab fluid to shallower depths, which supplied the primitive melts of UDMA plutonic rocks. The increase in the gradient and the decompression triggered melting of the juvenile lower crust (Fig. 12). Consequently, it is reasonable to suggest that the Golshekanan granitoid formed in an extensional setting and (or) transpression related to NE-wards subduction of the Neo-Tethys slab between Arabia and Eurasia.

7. Conclusions

The Golshekanan intrusive rocks are mostly granodiorite and granite, I-type affinity that crystallized at 37 Ma, based on the zircon U–Pb age. This body has low initial $^{87}Sr/^{86}Sr$ ratios and positive $\epsilon_{Nd}(t)$ values, and geochemical features indicative of derivation from juvenile crust rocks during late Eocene time, when the entire UDMA was probably under lithospheric extension, with thinning of continental lithosphere as a result of the Neo-Tethys oceanic rollback. Injection of hot mafic magma increased the geothermal gradient in the crustal root zone that was then responsible for partial melting of juvenile mafic bodies in the UDMA.

Declaration of interest. None.

References

Agard P, Omrani J, Jolivet L and Mouthereau F (2005) Convergence history across Zagros (Iran): constraints from collisional and earlier deformation. *International Journal of Earth Sciences* **94**, 401–19.

Agard P, Omrani J, Jolivet L, Whitechurch H, Vrielynck B, Spakman W, Monié P, Meyer B and Wortel R (2011) Zagros orogeny: a subduction-dominated process. *Geological Magazine* **148**, 692–725.

Ahmad T and Posht Kuhi M (1993) *Geochemistry and Petrogenesis of Urumiah–Dokhtar Volcanics Around Nain and Rafsanjan Areas: A Preliminary Study., Iranian.* Tehran: Ministry of Mines and Metals, Treatise on the Geology of Iran, 90 p.

Ahmadian J, Sarjoughian F, Lentz D, Esna-Ashari A, Murata M and Ozawa H (2016) Eocene K-rich adakitic rocks in the Central Iran: implications for evaluating its Cu–Au–Mo metallogenic potential. *Ore Geology Reviews* **72**, 323–42.

Ahmadzadeh G, Jahangiri A, Lentz D and Mojtahedi M (2010) Petrogenesis of Plio-Quaternary post-collisional ultrapotassic volcanism in NW of Marand, NW Iran. *Journal of Asian Earth Sciences* **39**, 37–50.

Alavi M (1994) Tectonics of the Zagros orogenic belt of Iran: new data and interpretations. *Tectonophysics* **229**, 211–38.

Alirezaei S and Hassanzadeh J (2012) Geochemistry and zircon geochronology of the Permian A type Hasanrobat granite, Sanandaj-Sirjan belt: a new record of the Gondwana break-up in Iran. *Lithos* **151**, 122–34.

Ao S, Xiao W, Khalatbari Jafari M, Talebian M, Chen L, Wan B, Ji W and Zhang Z (2016) U–Pb zircon ages, field geology and geochemistry of the Kermanshah ophiolite (Iran): From continental rifting at 79 Ma to oceanic core complex at ca. 36 Ma in the southern Neo-Tethys. *Gondwana Research* **31**, 305–18.

Asadi S (2018) Triggers for the generation of post-collisional porphyry Cu systems in the Kerman magmatic copper belt, Iran: New constraints from elemental and isotopic (Sr–Nd–Hf–O) data. *Gondwana Research* **64**, 97–121.

Azizi H and Asahara Y (2013) Juvenile granite in the Sanandaj–Sirjan Zone, NW Iran: late Jurassic–early Cretaceous arc–continent collision. *International Geology Review* **55**, 1523–40.

Babazadeh S, Ghorbani MR, Bröcker M, D'Antonio M, Cottle J, Gebbing T, Mazzeo FC and Ahmadi P (2017) Late Oligocene–Miocene mantle upwelling and interaction inferred from mantle signatures in gabbroic to granitic rocks from the Urumieh–Dokhtar arc, south Ardestan, Iran. *International Geology Review* **59**, 1590–608.

Babazadeh S, Ghorbani MR, Cottle JM and Bröcker M (2019) Multistage tectono-magmatic evolution of the central Urumieh–Dokhtar magmatic arc, south Ardestan, Iran: Insights from zircon geochronology and geochemistry. *Geological Journal* **54**, 2447–71.

Bahroudi A (1999) Geological Map of Shahrab. Scale 1:100 000. Tehran: Geological Survey of Iran.

Ballato P, Uba CE, Landgraf A, Strecker MR, Sudo M, Stockli DF, Friedrich A and Tabatabaei SH (2011) Arabia-Eurasia continental collision: Insights from late Tertiary foreland-basin evolution in the Alborz Mountains, northern Iran. *Geological Society of America Bulletin* **123**, 106–31.

Beard JS and Lofgren GE (1991) Dehydration melting and water-saturated melting of basaltic and andesitic greenstones and amphibolites at 1, 3, and 6.9 kb. *Journal of Petrology* **32**, 365–401.

Belousova E, Griffin WL, O'Reilly SY and Fisher NL (2002) Igneous zircon: trace element composition as an indicator of source rock type. *Contributions to Mineralogy and Petrology* **143**, 602–22.

Berberian F and Berberian M (1981) Tectono-plutonic episodes in Iran. In *Zagros-Hindu Kush-Himalaya Geodynamic Evolution* (eds HK Gupta and FM Delany), pp. 5–32. Washington, DC: American Geophysical Union.

Chappell BW and White AJ (1974) Two contrasting granite types. *Pacific Geology* **8**, 173–74.

Chekani Moghadam M, Tahmasbi Z, Ahmadi-Khalaji A and Santos JF (2018) Petrogenesis of Rabor-Lalehzar magmatic rocks (SE Iran): Constraints from whole rock chemistry and Sr-Nd isotopes. *Chemie der Erde* **78**, 58–77.

Chiu HY, Chung SL, Zarrinkoub MH, Mohammadi SS, Khatib MM and Iizuka Y (2013) Zircon U–Pb age constraints from Iran on the magmatic

evolution related to Neotethyan subduction and Zagros orogeny. *Lithos* **162**, 70–87.

Chiu HY, Chung SL, Zarrinkoub MH, Melkonyan R, Pang KN, Lee HY, Wang KL, Mohammadi SS and Khatib MM (2017) Zircon Hf isotopic constraints on magmatic and tectonic evolution in Iran: Implications for crustal growth in the Tethyan orogenic belt. *Journal of Asian Earth Sciences* **145**, 652–69.

Clemens JD and Stevens G (2012) What controls chemical variation in granitic magmas? *Lithos* **134–135**, 317–29.

Clemens JD, Stevens G and Farina F (2011) The enigmatic sources of I-type granites: the peritectic connexion. *Lithos* **126**, 174–181.

Daneshvar N, Maanijou M, Azizi H and Asahara Y (2019) Petrogenesis and geodynamic implications of an Ediacaran (550 Ma) granite complex (metagranites), southwestern Saqqez, northwest Iran. *Journal of Geodynamics* **132**, 101669.

Davoudzadeh M (1972) *Geology and Petrology of the area North of Nain, Central Iran.* Tehran: Geological Survey of Iran, 89 p.

Deng C, Wan B, Dong L, Talebian M, Windley BF, Dadashzadeh H, Mohammadi B and Barati B (2018) Miocene porphyry copper deposits in the Eastern Tethyan orogenic belt: Using Sr, O isotopes and Sr/Y ratios to predict the source of ore-related and ore-barren magmas. *Gondwana Research* **62**, 14–26.

Douce P (1999) Amphibolite to granulite transition in aluminous greywackes from the Sierra de Comechingones, Córdoba, Argentina. *Journal of Metamorphic Geology* **17**, 415–34.

Gromet P and Silver LT (1987) REE variations across the Peninsular Ranges batholith: Implications for batholithic petrogenesis and crustal growth in magmatic arcs. *Journal of Petrology* **28**, 75–125.

Guo F, Fan W, Li C, Gao X and Miao L (2009) Early Cretaceous highly positive εNd felsic volcanic rocks from the Hinggan Mountains, NE China: origin and implications for Phanerozoic crustal growth. *International Journal of Earth Sciences* **98**, 1395–411.

Gürsu S (2016) A new petrogenetic model for meta-granitic rocks in the central and southern Menderes Massif–W Turkey: Implications for Cadomian crustal evolution within the Pan-African mega-cycle. *Precambrian Research* **275**, 450–70.

Hacker BR, Kelemen PB and Behn MD (2015) Continental lower crust. *Annual Review of Earth and Planetary Sciences* **43**, 167–205.

Haschke M, Ahmadian J, Murata M and McDonald I (2010) Copper mineralization prevented by arc-root delamination during Alpine-Himalayan collision in central Iran. *Economic Geology* **105**, 855–65.

Hassanzadeh J, Stockli DF, Horton BK, Axen GJ, Stockli LD, Grove M, Schmitt AK and Walker JD (2008) U–Pb zircon geochronology of late Neoproterozoic–Early Cambrian granitoids in Iran: implications for paleogeography, magmatism, and exhumation history of Iranian basement. *Tectonophysics* **451**, 71–96.

Honarmand M, Rashidnejad Omran N, Neubauer F, Hashem Emami M, Nabatian G, Liu X, Dong Y, Quadt A and Chen B (2014) Laser-ICP-MS U–Pb zircon ages and geochemical and Sr-Nd–Pb isotopic compositions of the Niyasar plutonic complex, Iran: constraints on petrogenesis and tectonic evolution. *International Geology Review* **56**, 104–32.

Horton BK, Hassanzadeh J, Stockli DF, Axen GJ, Gillis RJ, Guest B, Amini A, Fakllari MD, Zamanzadeh SM and Grove M (2008) Detrital zircon provenance of Neoproterozoic to Cenozoic deposits in Iran: Implications for chronostratigraphy and collisional tectonics. *Tectonophysics* **451**, 97–122.

Jahn BM, Wu F and Chen B (2000a) Massive granitoid generation in Central Asia: Nd isotope evidence and implication for continental growth in the Phanerozoic. *Episodes* **23**, 82–92.

Jahn BM, Wu F and Hong D (2000b) Important crustal growth in the Phanerozoic: Isotopic evidence of granitoids from east-central Asia. *Journal of Earth System Science* **109**, 5–20.

Jahn BM, Valui G, Kruk N, Gonevchuk V, Usuki M and Wu JT (2015) Emplacement ages, geochemical and Sr-Nd–Hf isotopic characterization of Mesozoic to early Cenozoic granitoids of the Sikhote-Alin Orogenic Belt, Russian Far East: Crustal growth and regional tectonic evolution. *Journal of Asian Earth Sciences* **111**, 872–918.

Jiang ZQ, Wang Q, Wyman DA, Li ZX, Yang JH, Shi XB, Ma L, Tang GJ, Gou GN, Jia XH and Guo HF (2014) Transition from oceanic to continental

lithosphere subduction in southern Tibet: Evidence from the Late Cretaceous–Early Oligocene (~ 91–30 Ma) intrusive rocks in the Chanang–Zedong area, southern Gangdese. *Lithos* **196**, 213–31.

Kazemi K, Kananian A, Xiao Y and Sarjoughian F (2019) Petrogenesis of Middle-Eocene granitoids and their mafic microgranular enclaves in central Urmia-Dokhtar Magmatic Arc (Iran): Evidence for interaction between felsic and mafic magmas. *Geoscience Frontiers* **10**, 705–23.

Kazemi K, Kananian A, Yilin X and Sarjoughian F (2020) Role of magma mixing in generating of the Gheshlagh-Aftabrow intrusions, SW Buin-Zahra, Iran: Evidence for a juvenile origin from geochemical and Sr-Nd isotopic data. *Geological Journal* **55**, 253–79.

Kirkland C L, Smithies R H, Taylor R J M, Evans N and McDonald B (2015) Zircon Th/U ratios in magmatic environs. *Lithos* **212**, 397–414.

Kretz R (1983) Symbols for rock-forming minerals. *American Mineralogist* **68**, 277–79.

Kröner A, Kovach V, Belousova E, Hegner E, Armstrong R, Dolgopolova A, Seltmann R, Alexeiev DV, Hoffmann JE, Wong J and Sun M (2014) Reassessment of continental growth during the accretionary history of the Central Asian Orogenic Belt. *Gondwana Research* **25**, 103–25.

Li JX, Qin KZ, Li GM, Cao MJ, Xiao B, Chen L, Zhao JX, Evans NJ and McInnes BIA (2012) Petrogenesis and thermal history of the Yulong porphyry copper deposit, Eastern Tibet: insights from U-Pb and U-Th/He dating, and zircon Hf isotope and trace element analysis. *Mineralogy and Petrology* **105**, 201–21.

Liu Y, Hu Z, Gao S, Günther D, Xu J, Gao C and Chen H (2008) In situ analysis of major and trace elements of anhydrous minerals by LA-ICP-MS without applying an internal standard. *Chemical Geology* **257**, 34–43.

López S and Castro A (2001) Determination of the fluid absent solidus and supersolidus phase relationships of MORB-derived amphibolites in the range 4-14 kbar. *American Mineralogist* **86**, 1396–403.

Ludwig KR (2008) *A Geochronological Toolkit for Microsoft Excel.* Berkeley: Berkeley Geochronology Center, Special Publication.

Mansouri Esfahani M, Khalili M and Bakhshi M (2017) Petrogenesis of Soheyle-Pakuh and Golshekanan granitoid based on mineral chemistry of ferromagnesian minerals (north of Nain), Iran. *Journal of African Earth Sciences* **129**, 973–86.

Martin H (1987) Petrogenesis of Archaean trondhjemites, tonalites, and granodiorites from eastern Finland: major and trace element geochemistry. *Journal of Petrology* **28**, 921–53.

Middlemost EA (1994) Naming materials in the magma/igneous rock system. *Earth-Science Reviews* **37**, 215–24.

Mo X, Hou Z, Niu Y, Dong G, Qu X, Zhao Z and Yang Z (2007) Mantle contributions to crustal thickening during continental collision: evidence from Cenozoic igneous rocks in southern Tibet. *Lithos* **96**, 225–42.

Mohajjel M, Fergusson CL and Sahandi MR (2003) Cretaceous–Tertiary convergence and continental collision, Sanandaj–Sirjan zone, western Iran. *Journal of Asian Earth Sciences* **21**, 397–412.

Nazarinia A, Mortazavia M, Arvinb M, Hu R, Zhao C and Poosti M (2020) U-Pb zircon dating, Sr-Nd isotope and petrogenesis of Sarduiyeh granitoid in SE of the UDMB, Iran: implication for the source origin and magmatic evolution. *International Geology Review* **62**(13–14), 1796–814, doi: 10.1080/00206814.2018.1514668.

Nouri F, Azizi H, Stern R J, Asahara Y, Khodaparast S, Madanipour S and Yamamoto K (2018) Zircon U-Pb dating, geochemistry and evolution of the Late Eocene Saveh magmatic complex, central Iran: Partial melts of subcontinental lithospheric mantle and magmatic differentiation. *Lithos* **314–315**, 274–92.

Patiño Douce AEP (1999) What do experiments tell us about the relative contributions of crust and mantle to the origin of granitic magmas? In *Understanding Granites: Integratng New and Classical Techniques* (eds A Castro, C Fernandez and JL Vigneresse), pp. 55–75. Geological Society of London, Special Publication no. 168.

Pearce J (1996) Sources and settings of granitic rocks. *Episodes* **19**, 120–25.

Peng T, Zhao G, Fan W, Peng B and Mao Y (2014) Zircon geochronology and Hf isotopes of Mesozoic intrusive rocks from the Yidun terrane, Eastern Tibetan Plateau: petrogenesis and their bearings with Cu mineralization. *Journal of Asian Earth Sciences* **80**, 18–33.

Rapp RP and Watson EB (1995) Dehydration melting of metabasalt at 8–32 kbar: implications for continental growth and crust-mantle recycling. *Journal of Petrology* **36**, 891–931.

Ramezani J and Tucker RD (2003) The Saghand region, Central Iran: U-Pb geochronology, petrogenesis and implications for Gondwana tectonics. *American Journal of Science* **303**, 622–65.

Rezaei-Kahkhaei M, Galindo C, Pankhurst RJ and Esmaeily D (2011) Magmatic differentiation in the calc-alkaline Khalkhab–Neshveh pluton, Central Iran. *Journal of Asian Earth Sciences* **42**, 499–514.

Roberts MP and Clemens JD (1993) Origin of high-potassium, calc-alkaline, I-type granitoids. *Geology* **21**, 825–28.

Ross PS and Bédard JH (2009) Magmatic affinity of modern and ancient subalkaline volcanic rocks determined from trace-element discriminant diagrams. *Canadian Journal of Earth Sciences* **46**, 823–39.

Rossetti F, Nozaem R, Lucci F, Vignaroli G, Gerdes A, Nasrabadi M and Theye T (2015) Tectonic setting and geochronology of the Cadomian (Ediacaran- Cambrian) magmatism in central Iran, Kuh-e-Sarhangi region (NW Lut Block). *Journal of Asian Earth Sciences* **102**, 24–44.

Rudnick RL and Fountain DM (1995) Nature and composition of the continental crust: a lower crustal perspective. *Reviews of Geophysics* **33**, 267–309.

Rushmer T (1991) Partial melting of two amphibolites: contrasting experimental results under fluid-absent conditions. *Contributions to Mineralogy and Petrology* **107**, 41–59.

Sarjoughian F, Azizi M, Lentz DR and Ling W (2019) Geochemical and isotopic evidence for magma mixing/mingling in the Marshenan intrusion: Implications for juvenile crust in the Urumieh–Dokhtar Magmatic Arc, Central Iran. *Geological Journal* **54**, 2241–60.

Sarjoughian F, Javadi S, Azizi H, Ling W, Asahara Y and Lentz D (2020) Geochemical and Sr–Nd isotopic constraints on the genesis of the Soheyle-PaKuh granitoid rocks (central Urumieh-Dokhtar magmatic belt, Iran). *International Geology Review* **62**(13–14), 1769–95, doi: 10.1080/00206814.2019.1579676.

Sarjoughian F and Kananian A (2017) Zircon U-Pb geochronology and emplacement history of intrusive rocks in the Ardestan section, central Iran. *Geologica Acta* **15**, 25–36.

Sarjoughian F, Kananian A, Haschke M and Ahmadian J (2012) Geochemical signature of Eocene Kuh-e Dom shoshonitic dikes in NE Ardestan, Central Iran: implications for melt evolution and tectonic setting. *Journal of Geosciences* **57**, 241–64.

Sarjoughian F, Lentz D, Kananian A, Ao S and Xiao W (2018) Geochemical and isotopic constraints on the role of juvenile crust and magma mixing in the UDMB magmatism, Iran: evidence from mafic microgranular enclaves and cogenetic granitoids in the Zafarghand igneous complex. *International Journal of Earth Sciences* **107**, 1127–51.

Şengör AMC (1987) Cross-faults and differential stretching of hanging walls in regions of low angle normal faulting: examples from western Turkey. In *Continental Extensional Tectonics* (eds MP Coward, JF Dewey and PL Hancock), pp. 575–89. Geological Society of London, Special Publication no. 28.

Sepidbar F, Ao S, Palin RM, Li QL and Zhang Z (2019) Origin, age and petrogenesis of barren (low-grade) granitoids from the Bezenjan-Bardsir magmatic complex, southeast of the Urumieh-Dokhtar magmatic belt, Iran. *Ore Geology Reviews* **104**, 132–47.

Sepidbar F, Mirnejad H, Ma C and Moghadam HS (2018) Identification of Eocene-Oligocene magmatic pulses associated with flare-up in east Iran: Timing and sources. *Gondwana Research* **57**, 141–56.

Shabanian N, Davoudian A R, Dong Y and Liu X (2018) U-Pb zircon dating, geochemistry and Sr-Nd-Pb isotopic ratios from Azna-Dorud Cadomian metagranites, Sanandaj-Sirjan zone of western Iran. *Precambrian Research* **306**, 41–60.

Shafaii Moghadam H, Corfu F, Chiaradia M, Stern RJ and Ghorbani G (2014) Sabzevar Ophiolite, NE Iran: Progress from embryonic oceanic lithosphere into magmatic arc constrained by new isotopic and geochemical data. *Lithos* **210–211**, 224–41.

Shen P, Pan H, Cao C, Zhong S and Li C (2017) The formation of the Suyunhe large porphyry Mo deposit in the West Junggar terrain, NW China: Zircon

U–Pb age, geochemistry and Sr–Nd–Hf isotopic results. *Ore Geology Reviews* **81**, 808–28.

Shomali ZH, Keshvari F, Hassanzadeh J and Mirzaei N (2011) Lithospheric structure beneath the Zagros collision zone resolved by non-linear teleseismic tomography. *Geophysical Journal International* **187**, 394–406.

Simonetti A, Heaman LM, Chacko T and Banerjee NR (2006) In situ petrographic thin section U–Pb dating of zircon, monazite, and titanite using laser ablation–MC-ICP-MS. *International Journal of Mass Spectrometry* **253**, 87–97.

Soesoo A (2000) Fractional crystallization of mantle-derived melts as a mechanism for some I-type granite petrogenesis: an example from Lachlan Fold Belt, Australia. *Journal of the Geological Society* **157**, 135–49.

Stöcklin J (1968) Structural history and tectonics of Iran: a review. *AAPG Bulletin* **52**, 1229–58.

Sun SS and McDonough WS (1989) Chemical and isotopic systematics of oceanic basalts: implications for mantle composition and processes. In *Magmatism in the Ocean Basins* (eds AD Saunders and MJ Norry), pp. 313–45. Geological Society of London, Special Publication no. 42.

Tanaka T, Togashi S, Kamioka H, Amakawa H, Kagami H, Hamamoto T, Yuhara M, Orihashi Y, Yoneda S, Shimizu H, Kunimaru T, Takahashi K, Yanagi T, Nakano T, Fujimaki H, Shinjo R, Asahara Y, Tanimizu M and Dragusanu C (2000) JNdi-1: a neodymium isotopic reference in consistency with LaJolla neodymium. *Chemical Geology* **168**, 279–81.

Tang G J, Wang Q, Wyman D A, Chung S L, Chen H Y and Zhao ZH (2017) Genesis of pristine adakitic magmas by lower crustal melting: A perspective from amphibole composition. *Journal of Geophysical Research: Solid Earth* **122**, 1934–48.

Taylor SR and McLennan SM (1985) *The Continental Crust: Its Composition and Evolution.* Oxford: Blackwell, 312 p.

van Middelaar WT and Keith JD (1990) Mica chemistry as an indicator of halogen and oxygen fugacities in the CanTung and other W-related granitoids in the North American Cordillera. In *Ore-Bearing Granite Systems: Petrogenesis and Mineralizing Processes* (eds HJ Stein and JL Hannah), pp. 205–20. Geological Society of America, Special Paper no. 246.

Verdel C, Wernicke BP, Hassanzadeh J & Guest B (2011) A Paleogene extensional arc flare-up in Iran. *Tectonics* **30**(3), 0000, doi: 10.1029/2010TC002809.

Wan B, Deng C, Najafi A, Hezareh MR, Talebian M, Dong L, Chen L and Xiao W (2018) Fertilizing porphyry Cu deposits through deep crustal hot zone melting. *Gondwana Research* **60**, 179–85.

Wilson BM (1989) *Igneous Petrogenesis: A Global Tectonic Approach.* London: Unwin Hyman, London, 456 p.

Wu FY, Jahn BM, Wilde S and Sun DY (2000) Phanerozoic crustal growth: U–Pb and Sr–Nd isotopic evidence from the granites in northeastern China. *Tectonophysics* **328**, 89–113.

Wyllie PJ and Wolf MB (1993) Amphibolite dehydration-melting: sorting out the solidus. In *Magmatic Processes and Plate Tectonics* (eds HM Prichard, T Alabaster, NBW Harris and CR Neary), pp. 405–16. Geological Society of London, Special Publication no. 76.

Xiao L, Zhang HF, Clemens JD, Wang QW, Kan ZZ, Wang KM, Ni PZ and Liu XM (2007) Late Triassic granitoids of the eastern margin of the Tibetan Plateau: geochronology, petrogenesis and implications for tectonic evolution. *Lithos* **96**, 436–52.

Zhang D, Wei J, Fu L, Chen H, Tan J, Li Y, Shi W and Tian N (2015) Formation of the Jurassic Changboshan-Xieniqishan highly fractionated I-type granites, northeastern China: implication for the partial melting of juvenile crust induced by asthenospheric mantle upwelling. *Geological Journal* **50**, 122–38.

Zhang W, Chen H, Han J, Zhao L, Huang J, Yang J and Yan X (2016) Geochronology and geochemistry of igneous rocks in the Bailingshan area: Implications for the tectonic setting of late Paleozoic magmatism and iron skarn mineralization in the eastern Tianshan, NW China. *Gondwana Research* **38**, 40–59.

Zhao SQ, Tan J, Wei JH, Tian N, Zhang DH, Liang SN and Chen JJ (2015) Late Triassic Batang Group arc volcanic rocks in the northeastern margin of Qiangtang terrane, northern Tibet: partial melting of juvenile crust and implications for Paleo-Tethys ocean subduction. *International Journal of Earth Sciences* **104**, 369–87.

Zhu DC, Pan GT, Chung SL, Liao ZL, Wang LQ and Li GM (2008) SHRIMP zircon age and geochemical constraints on the origin of Lower Jurassic volcanic rocks from the Yeba Formation, southern Gangdese, South Tibet. *International Geology Review* **50**, 442–71.